Coordination Between Cytoplasmic and Envelope Densities Shapes Cellular Geometry in *Escherichia coli*

Griffin Chure[1, *], Roshali T. de Silva[1, 2], Richa Sharma[1], Michael C. Lanz[1,3], and Jonas Cremer[1, *]

[1]Department of Biology, Stanford University, Stanford, CA, USA
[2]Current Address: School of Life Sciences, Arizona State University, Tempe, AZ, USA
[3]Chan-Zuckerberg Biohub, San Francisco, CA, USA
[4]For correspondence: GC griffinchure@gmail.com; JC jonas.cremer@stanford.edu

April 7, 2025

Abstract

Microbes exhibit precise control over their composition and geometry in order to adapt and grow in diverse environments. However, the mechanisms that orchestrate this simultaneous regulation, and how they are causally linked, remains poorly understood. In this work, we derive and experimentally test a biophysical model of cell size regulation in *Escherichia coli* which relates the cellular surface-to-volume ratio to the total macromolecular composition and partitioning of the proteome between cellular compartments. Central to this model is the observation that the macromolecular density of the cytoplasm and the protein density within the cell membranes are maintained at a constant ratio across growth conditions. Using quantitative mass spectrometry, single-cell microscopy, and biochemical assays, we show this model quantitatively predicts a non-linear relationship between the surface-to-volume ratio, proteome localization, and the total ribosome content of the cell. This model holds under perturbations of intracellular ppGpp concentrations–thereby changing the ribosomal content–demonstrating that cellular geometry is not strictly determined by the cellular growth rate. These findings provide a biophysical link between the coregulation of proteome organization and cellular geometry, offering a quantitative framework for understanding bacterial size regulation across conditions.

1 Introduction

Microbial cells demonstrate remarkable phenotypic plasticity, simultaneously regulating their size as well as their macromolecular composition in concert with their growth rate across diverse conditions.[1] Research on this plasticity has largely proceeded along separate lines, resulting in a set of phenomenological "growth laws" that independently describe how composition[2–14] and geometry[15–26] scale with growth rate. This has been most prominently studied in the model bacterium *Escherichia coli* where the cellular ribosome content [Fig. S1(A)] and cell volume [Fig. S1(B)] scale approximately linearly and exponentially with the steady-state growth rate, respectively. Inspired by these strong phenomenological relations, several studies have interrogated their plausible interconnection,[27–29] yet we lack a unifying mechanistic framework that directly relates compositional and geometric regulation across diverse environments.

In this work, we integrate a systematic experimental dissection of compositional and geometric regulation in *E. coli* across growth conditions with biophysically-grounded mathematical modeling to establish a holistic, quantitatively predictive view of how proteomic composition and partitioning between cellular compartments jointly influence cellular geometry. Using quantitative mass spectrometry, we reveal a strong growth-rate dependence in how *E. coli* partitions its proteome between the cytoplasm, periplasm, and cell membranes. Specifically, we show that the cytoplasmic and periplasmic proteome partitions are strongly anti-correlated, suggesting a trade-off in localization between these compartments, while the membrane fraction of the proteome is constant across growth conditions. Given these relations, we propose that cell geometry is controlled such that the macromolecular densities within these compartments are tightly constrained. We present a biophysical model centered on this density-maintenance hypothesis that quantitatively describes how the surface-to-volume is directly dependent on the cellular composition, thereby providing a link between the phenomenological growth laws.

2 Results

2.1 Proteome Partitioning Between Cellular Compartments is Tightly Controlled and Condition Dependent

Interrogating the relationship between compositional and size regulation demands a self-consistent dataset where macromolecular composition, proteomic localization, cell geometry, and growth rates are simultaneously measured across different environmental conditions. Using the Gram-negative bacterium *E. coli* as a model system, we conducted a comprehensive suite of experiments to simultaneously measure these quantities in steady-state across seven different growth conditions defined by different carbon sources or mixes of carbon sources (described in Methods), yielding a data set highly-consistent with aggregated data from the literature [Fig. S2]. Leveraging recent advancements in quantitative mass spectrometry[30] and localization annotation of the *E. coli* proteome,[31] we queried how the *E. coli* proteome is partitioned between cellular compartments, namely the cytoplasm, periplasm, and membranes [Fig. 1(A)].

The fraction of the proteome partitioned to each compartment exhibits distinct scaling relationships with growth rate. The cytoplasmic proteome partition (ψ_{cyto}) increases approximately linearly as a function of the growth rate, ranging from $\sim 75\%$ to 85% of the total proteome [Fig. 1(B)]. In contrast, the periplasmic partition (ψ_{peri}) decreases with increasing growth rate, ranging from $\sim 15\%$ to 5% [Fig. 1(C)]. Notably, the partitioning of membrane-associated proteins (ψ_{mem}) remains approximately constant at $\sim 12\%$, exhibiting no significant dependence on growth rate [Fig. 1(D)]. This suggests that proteome localization is subject to global regulation beyond functional constraints. For example, since metabolic proteins–including enzymes and transporter components–are distributed across all compartments [Fig. S3], their allocation must be coordinated not just according to function but also spatially within the cell. This implies that localization dynamics are an integral part of cellular proteome regulation, rather than a passive consequence of metabolic demand.

The cytoplasmic and periplasmic partitioning trends are near-perfectly anticorrelated across growth rates [Fig. 1(E)], indicating a strong constraint in proteome balancing between these compartments. Further supporting this constraint, we find that the total partition of the proteome to these two compartments ($\psi_{cyto} + \psi_{peri}$) remains constant across all growth conditions, accounting for $\sim 87\%$ of the proteome mass

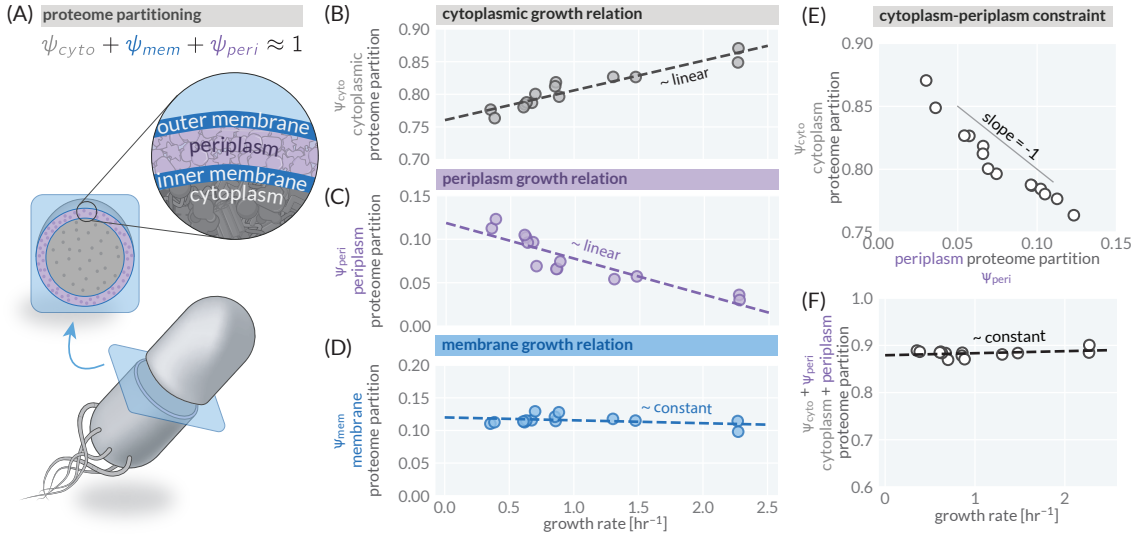

Figure 1: Proteomic partitioning and growth relations across *E. coli*'s cellular compartments. (A) *E. coli*'s three distinct, spatially separated compartments – the cytoplasm (gray), membranes (blue), and intermembrane space termed the periplasm (purple). The proteome is partitioned between these compartments. The mass fraction of the total proteome occupied by (B) the cytoplasm ψ_{cyto}, (C) the periplasm ψ_{peri}, and (D) inner and outer membranes ψ_{mem} as a function of the steady-state growth rate. Dashed lines represent empirical linear regressions on the data, with slopes as follows: $\psi_{cyto} \rightarrow\approx$ 0.05 hr^{-1}; $\psi_{peri} \rightarrow\approx$ - 0.04 hr^{-1}; $\psi_{mem} \rightarrow\approx -0.004$ hr^{-1}. (E) The linear trade-off correlation between the proteome allocation toward the cytoplasm and periplasm with a slope of ≈ -1. (F) The sum total proteome mass fraction of the cytoplasm and periplasm $\psi_{cyto} + \psi_{peri}$ as a function of the growth rate. Dashed line is a linear regression on the data with a slope of $\approx$ 0.004 hr^{-1}.

[Fig. 1(F)]. This observation highlights a fundamental trade-off in how cells structure their proteomes; any increase in cytoplasmic protein load is offset by a decrease in periplasmic protein load while the membrane protein partitioning remains unchanged.

2.2 Densities Within the Cytoplasm and Membranes Are Maintained Across Conditions

Trade-offs in proteome functional composition have been well studied in *E. coli*, particularly the competitive synthesis of metabolic and ribosomal proteins,[3,7,32,33] which affects biosynthetic fluxes and growth dynamics.[11,34,35] We propose that the trends shown in Fig. 1 illustrate that proteome partitioning across cellular compartments is governed by a qualitatively similar resource allocation constraint, but with a distinctly different underlying biophysical principle. In order to maintain macromolecular densities, which are critical in controlling biochemical reaction rates[36,37] and are thus subject to evolutionary optimization,[38–40] changes in proteome partitioning must be accompanied by compensatory changes in compartment size.

Using our direct measurements of cell size in addition to proteomic and bulk biochemical measurements (see Methods), we examined how, if at all, the macromolecular masses (Fig. S4) and densities (Fig. 2) within each compartment change across conditions. The cytoplasmic density ρ_{cyto}, comprised primarily by the total protein and RNA mass per unit cytoplasmic volume, remains moderately stable across conditions at approximately 400 fg / µm^3, with a weak linear dependence on growth rate [Fig. 2(A)]. Similarly, we find that the areal density of proteins within the membranes σ_{mem} is tightly constrained at approximately 3 fg / µm^2, with minimal variation across conditions [Fig. 2(B)]. In contrast, the periplasmic protein density exhibits a markedly different scaling behavior, decreasing from approximately 200 fg / µm^3 to 50 fg / µm^3 as a function of growth rate [Fig. 2(C)]. Despite this steep decline in periplasmic density, the total mass of

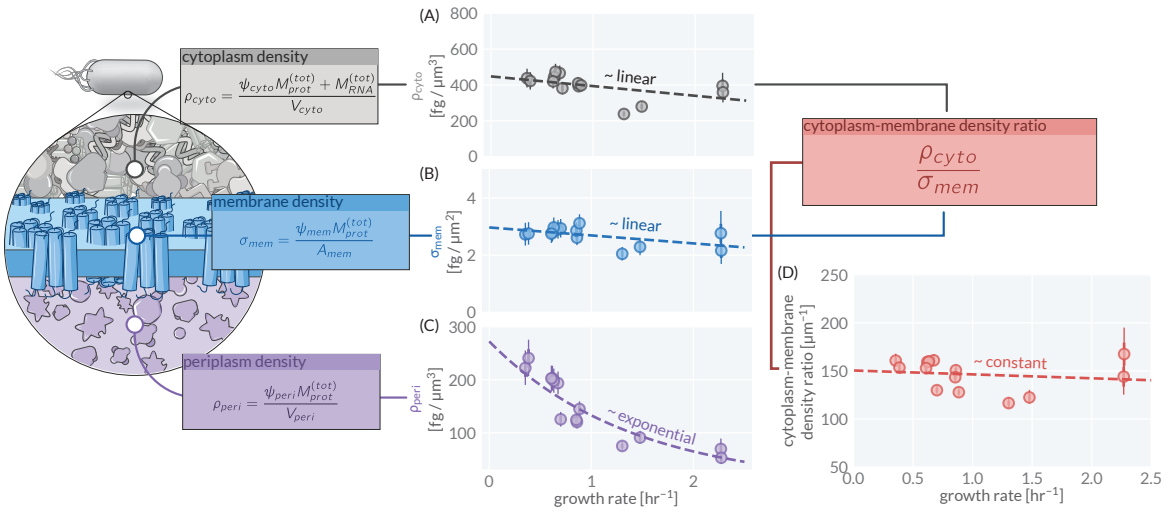

Figure 2: Macromolecular densities within cellular compartments are tightly regulated. The major macromolecular densities as a function of the growth rate in (A) the cytoplasm, (B) the membranes, and (C) the periplasmic space. (D) The ratio of the cytoplasmic and membrane densities as a function of the growth rate. Points calculated from mass spectrometry data as described in boxes. Total protein mass $M_{prot}^{(tot)}$ and total RNA mass $M_{RNA}^{(tot)}$ per cell for each sample was empirically determined from independent quantification as described in the Appendix. Points represent the mean value of the posterior probability distribution for each quantity. Extent of the thin and thick error bars correspond to the 95% (approximately 2σ) and 68% (approximately 1σ) credible regions of the posterior distribution, respectively. Dashed lines represent fits to the mean values.

periplasmic proteins per cell remains constant at approximately 20 fg for all growth conditions [Fig. S4(E)]. This observation suggests that periplasmic protein load, rather than the density, is homeostatically maintained.

While both the cytoplasmic density and membrane protein density exhibit slight negative linear dependencies on growth rate, their ratio remains constant across conditions [Fig. 2(D)]. Given the prevalence of interfacial biochemical interactions between the cytoplasm and the membranes, deviations from a constant density ratio likely imposes large physiological costs. Thus, it is plausible that pressure to maintain this density ratio influences cell geometry.

2.3 Deriving a Model of Density Maintenance

To better understand the constraints that a constant cytoplasm-membrane density [Fig. 2(D)] imposes on cell geometry, we can mathematically examine how each density is defined. We make the well-motivated assumption that the majority of the cytoplasmic biomass is composed of protein and RNA,[41] yielding the cytoplasmic density

$$\rho_{cyto} = \frac{\psi_{cyto} M_{prot}^{(tot)} + M_{RNA}^{(tot)}}{V_{cyto}}, \tag{1}$$

where ψ_{cyto} represents the cytoplasmic proteome partition, $M_{prot}^{(tot)}$ is the total protein mass per cell, $M_{RNA}^{(tot)}$ is the total RNA mass per cell, and V_{cyto} is the total cytoplasmic cell volume, defined as the total cellular volume V less the periplasmic volume, $V_{cyto} = V - V_{peri}$. Similarly, we define the areal density of proteins within the cell membranes σ_{mem} as

$$\sigma_{mem} = \frac{\psi_{mem} M_{prot}^{(tot)}}{A_{mem}}, \tag{2}$$

where ψ_{mem} denotes the membrane proteome partition and A_{mem} is the total membrane area of the cell, including both inner and outer membranes.

We now introduce two simplifications. First, we consider that the total cytoplasmic volume V_{cyto} is sufficiently larger than the total periplasmic volume V_{peri}, such that $V_{cyto} \approx V$. Second, we assume that the inner and outer membranes are narrowly spaced (measured periplasmic widths are ≈ 25 nm[42]) so that the total membrane area is approximately twice the measured cell surface area, $A_{mem} \approx 2S_A$.

Applying these simplifications and taking the ratio of Eq. 1 and Eq. 2 yields an expression for the cytoplasm-membrane density ratio κ:

$$\kappa \equiv \frac{\rho_{cyto}}{\sigma_{mem}} = \frac{\psi_{cyto} M_{prot}^{(tot)} + M_{RNA}^{(tot)}}{V} \times \frac{2S_A}{\psi_{mem} M_{prot}^{(tot)}} = \frac{2\left(\psi_{cyto} + \frac{M_{RNA}^{(tot)}}{M_{prot}^{(tot)}}\right)}{\psi_{mem}} \times \frac{S_A}{V}. \tag{3}$$

This expression makes explicit the dependence of κ on both the surface-to-volume ratio S_A/V, a quantity proposed as a "state variable" for bacterial morphogenesis,[22] and the RNA-to-protein ratio $M_{RNA}^{(tot)}/M_{prot}^{(tot)}$, a key determinant of growth rate and a core component of the nutrient growth law.[43] The density ratio κ thus acts as a scaling factor linking cellular geometry to proteome partitioning and macromolecular composition, embedding both geometric and biosynthetic constraints.

Given that proteins are partitioned among three compartments (Fig. 1(A), $\psi_{cyto} + \psi_{mem} + \psi_{peri} \approx 1$) and that the RNA-to-protein ratio is directly related to the ribosomal fraction of the total proteome (termed the *ribosomal proteome allocation* ϕ_{rib}) with a proportionality constant β (see Appendix), Eq. 3 can be rewritten as

$$\frac{S_A}{V} = \frac{\kappa \psi_{mem}}{2\left(1 - \psi_{mem} - \psi_{peri} + \beta\phi_{rib}\right)}, \tag{4}$$

which expresses the cellular geometry in terms of the proteome partitioning and the proteomic allocation towards ribosomes.

2.4 Measurements of Surface-to-Volume and Proteomic Composition Agree With Theoretical Predictions

Equation 4, schematized in Fig. 3(A), provides a quantitative prediction for how the cellular geometry, defined by the surface-to-volume ratio S_A/V, scales with the composition and localization of the proteome under the assumption that the cytoplasm-to-membrane density ratio κ remains constant. In particular, this framework predicts that S_A/V is determined by the proteome fraction partitioned to membranes ψ_{mem} and the periplasm ψ_{peri}, and the ribosomal proteome allocation ϕ_{rib}, linking cell size regulation directly to proteome composition. We sought to determine whether the observed S_A/V follows the expected non-linear dependence on ϕ_{rib} as prescribed by Eq. 4.

Theoretical and experimental dissections of the nutrient growth law[3,7,8,11] have established that the ribosomal proteome fraction ϕ_{rib} increases from approximately 5% to 30% of the total proteome from slow to fast growth conditions, respectively [Fig. S1(A)]. If ϕ_{rib} serves as a control variable for growth, then our density maintenance model predicts a corresponding non-linear scaling of S_A/V. However, accurately making this prediction requires empirical knowledge of how ψ_{peri} and ψ_{mem} change as a function of ϕ_{rib}. Using our mass spectrometry measurements, we characterized these dependencies and found that ψ_{mem}

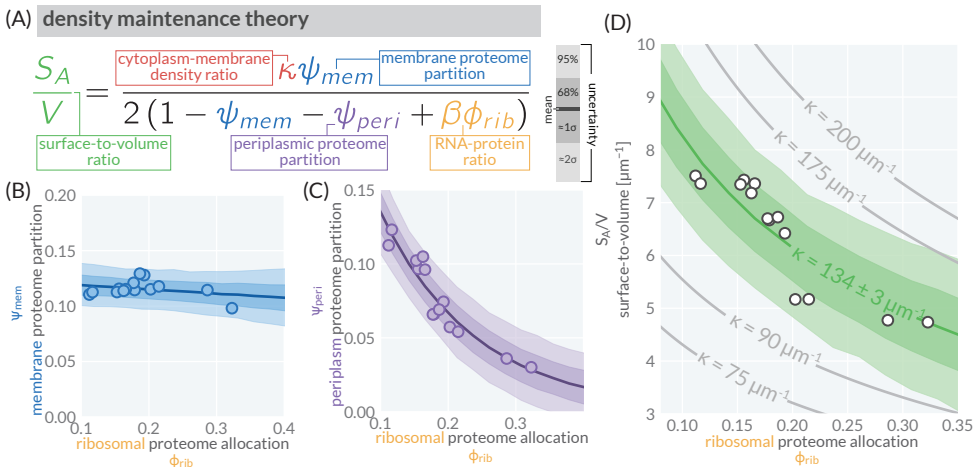

Figure 3: A density maintenance theory quantitatively predicts scaling between surface-to-volume ratio (S_A/V) and proteome allocation towards ribosomes ϕ_{rib}. (A) The density maintenance theory as derived in the text with the density ratio κ, membrane proteome partition ψ_{mem}, periplasmic proteome partition ψ_{peri}, and RNA/protein ratio $\beta\phi_{rib}$ highlighted in red, blue, purple, and gold, respectively. (B) The empirical linear (approximately constant) relationship between membrane proteome partition and ribosomal proteome allocation. (C) The empirical exponential relationship between periplasmic proteome partition and ribosomal proteome allocation. (D) Predicted scaling of surface-to-volume S_A/V on the ribosomal proteome allocation ϕ_{rib} for different values of the density ratio κ (grey lines). Green curves correspond to fit of Eq. 4 to our data, using the empirical relationships shown in (B) and (C). Lines correspond to the mean value of the posterior predictive distribution. Shaded bands correspond to the 95% (pale, approximately 2σ) and 68% (light, approximately 1σ) credible regions of the posterior predictive distribution for each quantity. White-faced points correspond to our direct measurements of allocation parameters via mass spectrometry and S_A/V via microscopy.

remains nearly constant, while ψ_{peri} exhibits an approximately exponential decline as a function of ϕ_{rib} [Fig. 3(B, C)]. Using a Bayesian inferential model to quantify our uncertainty (Methods and Appendix), we parameterized these relationships and integrated them into our theoretical predictions.

We then evaluated Eq. 4 under different candidate values for κ and found that the predicted S_A/V exhibits a strong non-linear dependence on ϕ_{rib} [Fig. 3(D), grey lines], covering a physiologically plausible range of values for S_A/V between ≈ 3 and 10 μm^{-1}. Using a Bayesian statistical model, we inferred the best-fit value of $\kappa = 134 \pm 3$ μm^{-1} to our direct measurements of S_A/V [Fig. 3(D), markers and green bands]. We find that this model describes our observations with notable quantitative accuracy.

2.5 Perturbations of Intracelluar ppGpp Concentrations Predictably Alter Cell Geometry

Fig. 3 suggests that the surface-to-volume ratio S_A/V can be accurately described by a simple model defined by a constant cytoplasm-membrane density ratio κ and a variable ribosomal allocation ϕ_{rib}. Our data thus far comes from cells grown in different carbon sources with a range of growth rates, and therefore a range of ϕ_{rib}. However, our model (Eq. 4) does not explicitly depend on the cellular growth rate nor the specifics of the environment. To confirm this independence, we perturbed ϕ_{rib} within a single nutrient condition by modulating the intracellular concentration of the global regulator guanosine tetraphosphate (ppGpp),[6,44] and measured the consequences on cell size and proteomic composition.

To systematically alter ppGpp levels, we employed a genetic system developed by Büke et al.[45] that enables tunable expression of RelA and MeshI, enzymes that synthesize and degrade ppGpp, respectively [Fig. 4(A)]. By titrating the expression of these enzymes in two growth conditions – glucose and glucose supplemented with casamino acids (glucose+CAA) – we directly measured the resulting changes in proteomic

composition, partitioning, growth rate, and surface-to-volume ratio. Under Eq. 4, we would expect that increasing ppGpp levels would decrease ϕ_{rib}, leading to an increase in S_A/V, while decreasing ppGpp should have the opposite effect. Since ribosome content is typically growth-optimized within a given condition,[11] these perturbations also provide a test of whether Eq. 4 correctly predicts S_A/V independently of growth rate.

Inducing the expression of MeshI, which decreases ppGpp, or RelA, which increases ppGpp, altered ribosomal proteome allocation ϕ_{rib} [Fig. 4(B)], growth rate [Fig. 4 (C)], and surface-to-volume ratio [Fig. 4(D)] in the qualitatively predicted directions. Specifically, induction of MeshI or RelA altered the ribosomal proteome allocation ϕ_{rib} as anticipated, with corresponding shifts in growth rate and S_A/V in both growth conditions [Fig. 4(B)]. These results confirm that the ppGpp perturbations directly modulate ribosomal allocation and allow us to assess their impact on cell geometry independent of the growth rate [Fig. S5(A)].

To quantitatively compare the predicted and measured S_A/V under ppGpp perturbations, we determined the partitioning and allocation parameters in Eq. 4 from mass spectrometry measurements and assumed that κ remains fixed at the inferred value of $\kappa = 134 \pm 3$ μm^{-1} [Fig. 3(D)]. For MeshI induction [Fig. 4(E), (ii) $\rightarrow$ (i)], the predicted and measured S_A/V are in strong quantitative agreement for both glucose and glucose+CAA conditions, with values falling within experimental variation of the wild-type strain. For RelA induction [Fig. 4(F), (iii) $\rightarrow$ (iv) $\rightarrow$ (v)], we find that predicted and measured S_A/V agree well within the glucose+CAA condition but diverge in the glucose-only condition at high RelA expression levels. In this scenario, Eq. 4 predicts $S_A/V \approx 12$ μm^{-1}, which deviates significantly from the measured values of $S_A/V \approx 7$ [Fig. 4(D)]. We hypothesize that RelA induction in glucose pushes the system into a regime where maintenance of a constant density ratio is not physiologically possible. Indeed, empirical measurements of the cytoplasm-membrane density ratio under these conditions [Fig. S5(B), see Methods] reveal a decrease to approximately 100 μm^{-1}. This suggests that the assumption of a constant density ratio breaks down due to a physical upper bound in $S_A/V \approx 8$ μm^{-1} (dashed line). Given a rod-shaped bacterium, this S_A/V corresponds to a cell width $w \approx 0.5$ μm, in line with the reported observed minimum width of *E. coli* [Fig. S2(E)]. Maintaining a constant density ratio for the high RelA induction conditions in glucose would require cells to adopt a width of ≈ 0.25 μm, well below this physiological limit. This establishes a boundary of validity for the density maintenance model, providing insight into the range of conditions under which proteome composition alone can predict cellular geometry.

3 Discussion

In this work, we take a holistic approach towards understanding the interconnections between cellular composition, proteome localization, and cellular geometry. We propose a concrete, biophysical principle that lies at the center of this regulation – that macromolecular densities within the cytoplasm and the areal density of proteins in the cell membrane are maintained within a narrow range. This constraint emerges from simultaneous control over the size of each cellular compartment and the partitioning of the proteome between them. Motivated by these observations, we derive a simple mathematical model that quantitatively relates the cellular geometry, namely the surface-to-volume ratio, to the partitioning of the proteome between compartments and the functional composition of the proteome, principally the proteome fraction composed of ribosomes. We conducted a suite of experiments measuring steady-state growth rate, cell size,

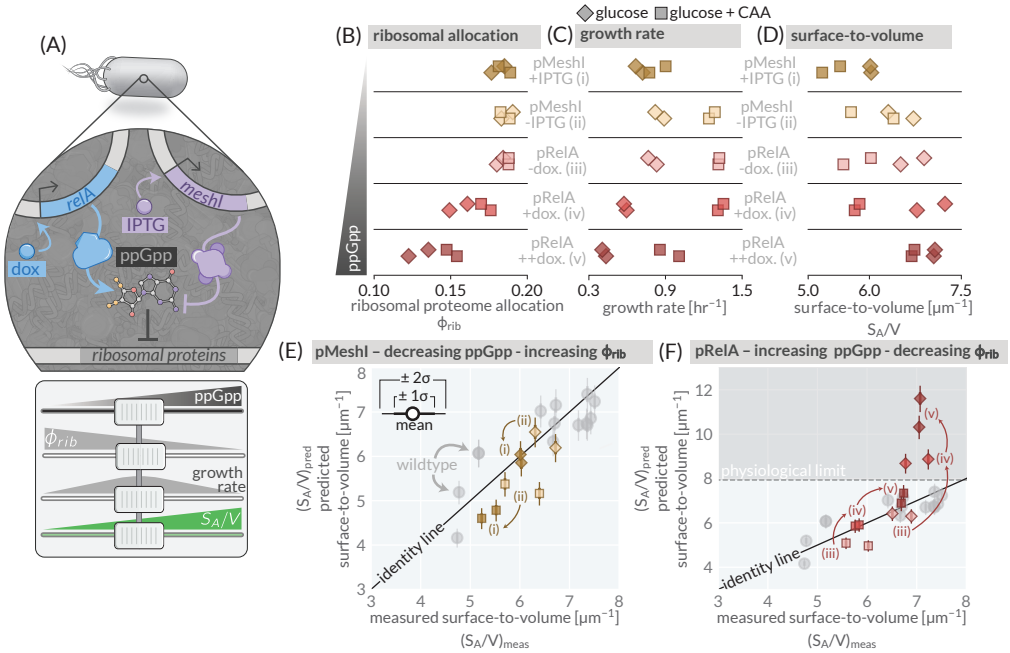

Figure 4: Perturbing intracellular ppGpp predictably alters the surface-to-volume ratio. (A, top) The genetic system as adapted from Büke *et al.*,[45] allowing for inducible control over intracellualr ppGpp concentrations. (A, bottom) The expected effect of RelA or MeshI induction on ppGpp concentration, ribosomal proteome allocation, growth rate, and the surface-to-volume ratio. Observed effects of MeshI/RelA induction on (B) ribosomal allocation, (C) growth rate, and (D) surface-to-volume ratio in a glucose (diamonds) or casamino acid supplemented glucose growth medium (squares). The predicted versus measured S_A/V for MeshI (E, gold markers) and RelA (F, red markers) induction conditions. Gray circles correspond to the wildtype strain in different growth conditions. Thin and tick error bars correspond to the 95% ($\approx 2\sigma$) and 68% ($\approx 1\sigma$) credible regions of the posterior distribution for the surface-to-volume assuming a constant density ratio κ inferred in Fig. 3(C). MeshI was induced with IPTG ($-$: 0 μM $+$: 100 μM,) and RelA was induced with doxycyline ($-$: 0 ng/mL; $+$: 2 ng/mL, $++$: 4 ng/mL).

and proteome composition across a broad range of conditions and genetic perturbations. To our knowledge, this is the only data set with simultaneous measurements of these quantities with sufficient statistical power to test our biophysical model. Using this data set, we demonstrate that this model of density maintenance quantitatively predicts how the surface-to-volume ratio is dependent on the steady-state proteome composition and localization. As such, this approach demonstrates that cell composition, rather than bulk growth rate, is a major determining factor of cell size control.

Beyond our own observations, we find that this picture stands in good agreement with the literature examining what does (and does not) alter cell size across conditions. For example, Basan *et al.*[28] utilized the strong over-expression of a non-needed cytoplasmic protein, to drastically change composition. As anticipated by our theory, the authors report that width and the average cell size increased considerably while total drymass density was maintained. Furthermore, as our theory does not include any rate parameters or binding constants, we would expect its predictions to be independent of temperature. Indeed, this is consistent with previous studies showing that cell composition and size are both well-maintained across wide temperature ranges, while the growth rate is strongly temperature dependent.[43,46–50] Finally, while we focus in this work on *E. coli*, there is evidence that density maintenance may be a more general property across the microbial world. For example, recent work in *Corynebacterium glutamicum*,[51] a gram-positive bacterium, reveals a strong correlation between the surface-to-volume ratio and the RNA-to-protein ratio that is consistent with our theoretical predictions. Similarly, the methanogenic archaeon *Methanococcus maripaludis* demonstrates a fixed composition across growth conditions and, in line with our theory, a constant cell size.[52] In total, a hypothesis that cells prioritize the maintenance of macromolecular densities and do so through control of cell geometry is strongly supported by a litany of observations which have at times seemed incongruous.

Recently, Büke et al.[45] demonstrated that ppGpp directly altered average cell volume in a manner that was uncoupled from the bulk growth rate. While unequivocally establishing a relationship between ppGpp concentration and cell size, the precise mechanism underlying this connection remains unclear. Our hypothesis of density maintenance provides a natural explanation—intracellular ppGpp pools modulate ribosomal content by regulating the expression of ribosomal rRNA and protein genes, thereby altering cellular composition and, in turn, cell geometry. Other work by Harris & Theriot[22] has proposed that the surface-to-volume ratio is a quantity that cells actively monitor and homeostatically control through the coordination of volume and surface expansion. Our work builds upon this idea by providing a plausible biophysical principle by which S_A/V can be regulated, as illustrated in Panel A of Fig. 5. Throughout the cell cycle, rod-shaped bacterial cells maintain a fixed width while their length increases, and so long as the length remains significantly larger than the width ($\ell \gg w$), the surface-to-volume ratio follows the simple relation $S_A/V \approx 4/w$. This implies that rather than directly monitoring both surface area and volume, cells could achieve robust control over S_A/V simply by regulating their width. Under this framework, maintaining a constant density ratio κ provides a natural feedback mechanism linking biochemical composition to morphological regulation, ensuring that cell geometry is tuned to maintain homeostasis across different conditions.

This model begs two fundamental molecular questions: how could cells sense densities and how is sensing coupled to width control? We speculate that the Rod complex lies at the heart of both of these questions. The Rod complex is a large protein assembly[53–55] found across the bacterial tree of life,[56] which rotates about the long axis of the cell along the inner membrane expanding the cell wall and, therefore,

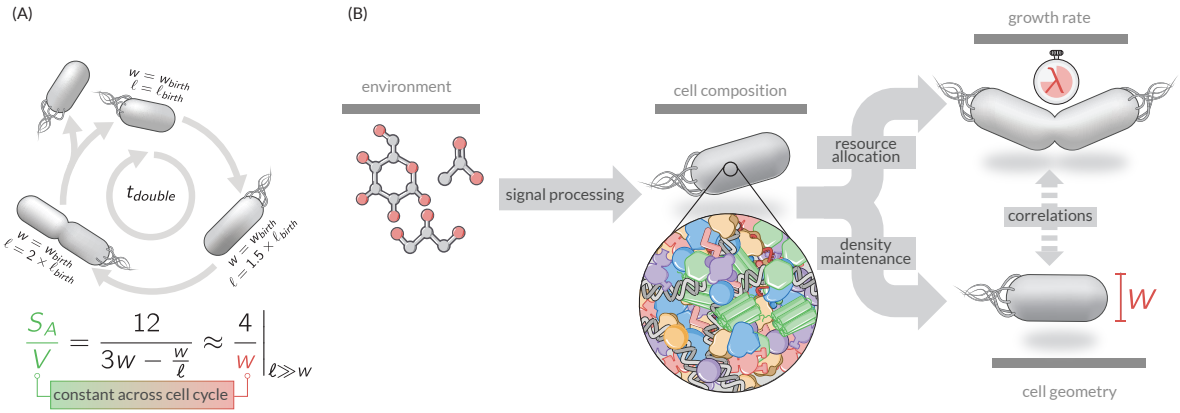

Figure 5: Growth rate as an emergent property of compositional and geometric regulation. (A) The cell length changes over the course of the cell cycle, approximately doubling the cell volume, but the cell width remains approximately constant within a given growth condition. The S_A/V (bottom) of a rod-shaped cell is therefore approximately constant across the cell cycle. (B) Chemical details of the environment set the cellular composition through sensory pathways and integrated regulation of gene expression. Given the cellular composition, the bulk growth rate is determined via the regulation of metabolic and translational fluxes, setting cellular composition. Simultaneously and following our density maintenance theory pressure to constrain macromolecular densities within the cytoplasm and membrane protein densities within the membrane determines cellular geometry.

increasing the cell volume and surface area.[57,58] While lengthening the cell over the course of the cell cycle, the Rod complex also determines the width of the cell,[54,59,60] thereby controlling the surface-to-volume ratio. Thus, for densities in the cytoplasm and membrane to be effectively maintained, the activity of the Rod complexes must be controlled accordingly. As the Rod complex rotates through both the cytoplasmic and membrane environments, it is subjected to density-dependent forces. We thus think it is plausible that the action of the Rod complex is modulated by membrane and cytoplasmic densities to ensure coordination of length increase and width control. As genetic perturbations of various Rod complex components have been shown to strongly affect cell size and shape homeostasis,[60,61] we speculate that they may together act also as “sensor" of the relative density between the membrane and cytoplasm.

Despite evidence that growth rate regulation and cell size control are uncoupled in various situations– such as through temperature variation– growth rate is commonly viewed as a control variable for bacterial physiology as a whole. However, we argue that growth should be thought of as an emergent property of the cellular physiology, as is cell size. We view the cell composition as being set by the coordination of gene expression following from sensing of the cells’ environment and its metabolic state. Growth rate emerges from the relative rates of metabolism and translation resulting from this composition.[11] Separately, as we have demonstrated in this work, the pressure to maintain macromolecular densities within the cytoplasm and membrane compartments strongly constrains the cellular geometry. As a consequence, strong correlations between cell size and growth rate can emerge even without a direct causal link between them [Fig. 5(B)]. Thus, approaches to understand cell physiology should not rely on growth rate as an explanatory process, but rather the fundamental physical and chemical limits that cells must obey and can plausibly biochemically measure.

4 Methods

4.1 Bacterial Strains and Cell Husbandry

Experiments performed in this work were conducted using *Escherichia coli* K-12 strain NCM3722 supplied from the laboratory of Terence Hwa at UCSD, originally obtained from the laboratory of Sydney Kustu.[62] Perturbations of intracellular ppGpp concentrations were performed using a genetic system as described in Büke *et al.*[45] These plasmids (without fluorescent tags) were ordered from AddGene (pRelA' AddGeneID:175595; pMeshI AddGeneID:175594) and transformed individually into our lab stock of NCM3722 on appropriate selection conditions. All used strains are listed in Appendix Table 2. Culturing plasmids were performed under either Ampicillin (pMeshI; 100 µg / mL) or Kanamycin (pRelA; 50 µg/mL) selection.

To ensure sample analysis at steady-state, cells were processed through three different cultivation steps before samples were taken. To start, "seed culture" was grown in Miller LB rich medium (Fisher Scientific, Cat. No. BP1426) from a single colony on an LB agarose plate. This seed culture was grown in a 37° C waterbath shaker under constant aeration (shaking at 240 rpm) for several hours until the culture was saturated. This seed culture was then diluted at least three hundred fold into fresh LB media or a minimal phosphate buffer medium (5.7 mM K_2SO_4, 77.6 mM KH_2PO_4, 34.6 mM KH_2PO_4, 400 µM $MgSO_4$, 43.1 mM NaCl, 10 mM NH_4Cl) supplemented with a carbon source (either 30 mM acetate, 10 mM sorbitol, 10 mM glycerol, or 10 mM glucose) or mix of carbon sources (glucose + acetate or glucose + 0.1% w/v casamino acids). This culture, the "pre-culture condition", was then allowed to grow under constant aeration until an optical density $OD_{600nm} \approx 0.3 - 0.4$ (Thermo Scientific Genesys 30, 1-cm path length cuvette) was reached. This culture was the diluted ten fold into 15 mL of fresh medium with the same composition, pre-warmed to 37° C. This culture, the "experimental culture", was then grown in identical conditions as the pre-culture. Growth curves were obtained by regular OD_{600} measurements while the culture remained between an optical density range of $OD_{600nm} \approx 0.04 - 0.5$. For strains with ppGpp perturbations, the seed culture was grown in a glucose-supplemented minimal medium. Once the seed culture reached an optical density OD_{600nm} between $0.3 - 0.4$, the culture was diluted two-thousand fold into a fresh, prewarmed glucose minimal medium supplemented with the appropriate amount of inducer, either doxycycline (dox, Sigma, Cat. No. D5207) or Isopropyl β- d-1-thiogalactopyranoside (IPTG, Goldbio Cat. No. 12481C5) for RelA and MeshI induction, respectively.

During the growth of the experimental culture, samples were taken and processed for cell size measurement and mass spectrometry as described briefly below. All cultivation steps were performed in glass tubes with at least four volumes of head space for sufficient gas exchange and aerobic growth.

4.2 Quantification of Cell Size

From a steady-state culture, 2 µL was transferred onto a 1% agarose pad supplemented with isotonic mimimal medium buffer base. After drying for 2 - 3 minutes, this pad was mounted on a slide, covered with a coverslip, and imaged under 100X phase-contrast microscopy using a Zeiss AxioVert 200M microsope outfitted with an AmScope MU1003 CMOS camera. Images were transferred to a back-up server and were later processed using in-house image processing Python code, as described in the Appendix.

4.3 Proteome Quantification via Mass Spectrometry

Cultures were grown to a final $OD_{600nm} \approx 0.4 - 0.5$ and were then harvested for proteomic analysis. An aliquot of 12 mL of the steady-state culture was removed from the culture vessel and transferred to a 14 mL centrifuge tube. Cells were pelleted at 3000 $\times g$ for 10 min at 4 °C. All but 1 mL of the supernatant was carefully decanted and transferred to a clean 14 mL centrifuge tube. The pellet was resuspended in the residual 1 mL of supernatant and transferred to a 1.5 mL eppendorf tube and pelleted at 3000 $\times g$ for 1 min at 4 °C. The supernatant was removed and added to the decanted supernatant and thoroughly mixed. The OD_{600nm} of this pooled supernatant was recorded to correct for cell loss. The pellet was then frozen at -80 °C for later proteomic analysis.

When ready for proteomic processing, pellets were removed from the -80 °C and thawed on ice. The pellets were then resuspended in a denaturation/reduction buffer (0.07M Tris-Cl, 5% (v/v) mercaptoethanol, 0.6% (w/v) SDS and 15% (v/v) glycerol) by boiling for 10 min at 95 °C with intermittent vortexing. Debris was pelleted by centrifugation for 10 minutes (10,000 $\times g$). Cleared supernatants were alkylated with 5mM iodoacetamide, and then precipitated with three volumes of a solution containing 50% acetone and 50% ethanol. Proteins were re-solubilized in 2 M urea, 50 mM Tris-HCl, pH 8.0, and 150 mM NaCl, and then digested with TPCK-treated trypsin (50:1) overnight at 37 °C. Trifluoroacetic acid and formic acid were added to the digested peptides for a final concentration of 0.2%. Peptides were desalted with a Sep-Pak 50mg C18 column (Waters). The C18 column was conditioned with 500 µL of 80% acetonitrile and 0.1% acetic acid and then washed with 1000 µL of 0.1% trifluoroacetic acid. After samples were loaded, the column was washed with 2000 µL of 0.1% acetic acid followed by elution with 400 µL of 80% acetonitrile and 0.1% acetic acid. The elution was dried in a Concentrator at 45 °C. De-salted peptides were resuspended in 0.1% Formic acid.

For each sample, 25 µg of desalted peptide samples were resuspended in 20 µL of 100 mM Triethylammonium bicarbonate solution and labeled with 16-plex TMTpro at a ratio 4:1 (TMT:peptide). Total reaction volume was less than 25 µL. The labeling reaction was quenched with a final concentration of 0.5% hydroxylamine for 15 min. Labeled peptides were pooled and acidified to pH $\sim$ 2 using drops of 10% TFA. Excess TMT label was removed by re-running the pooled sample through a Sep-Pak 50-mg C18 column (as described above).

TMT-labeled peptides were resuspended in 0.1% formic acid analyzed on a Fusion Lumos mass spectrometer (Thermo Fisher Scientific, San Jose, CA) equipped with a Thermo EASY-nLC 1200 LC system (Thermo Fisher Scientific, San Jose, CA). Peptides were separated by capillary reverse phase chromatography on a 25 cm column (75 µm inner diameter, packed with 1.6 µm C18 resin, AUR2-25075C18A, Ionopticks, Victoria Australia). Peptides were introduced into the Fusion Lumos mass spectrometer using a 180-min stepped linear gradient at a flow rate of 300 nL / min. The steps of the gradient are as follows: 6–33% buffer B (0.1% (v:v) formic acid in 80% acetonitrile) for 145 min, 33-45% buffer B for 15min, 40–95% buffer B for 5 min and maintain at 90% buffer B for 5 min. The column temperature was maintained at 50 °C throughout the procedure. Xcalibur software (v.4.4.16.14) was used for the data acquisition and the instrument was operated in data-dependent mode. Advanced peak detection was disabled. Survey scans were acquired in the Orbitrap mass analyzer (centroid mode) over the range 380–1,400 m/z with a mass resolution of 120,000 (at m/z 200). For MS1, the normalized AGC target (%) was set at 250 and maximum injection time was set to 100 ms. Selected ions were fragmented by collision-induced dissociation (CID)

with normalized collision energies of 34 and the tandem mass spectra were acquired in the ion trap mass analyzer with the scan rate set to 'Rapid'. The isolation window was set to the 0.7 m/z window. For MS2, the normalized AGC target (%) was set to 'Standard' and maximum injection time to 35 ms. Repeated sequencing of peptides was kept to a minimum by dynamic exclusion of the sequenced peptides for 30 s. The maximum duty cycle length was set to 3 s. Relative changes in peptide concentration were determined at the MS3 level by isolating and fragmenting the five most dominant MS2 ion peaks.

All raw files were searched using the Andromeda engine embedded in MaxQuant (v2). Reporter ion MS3 search was conducted using TMTpro (16-plex) isobaric labels. Variable modifications included oxidation (M) and protein N-terminal acetylation. Carbamidomthyl (C) was a fixed modification. The number of modifications per peptide was capped at five. Digestion was set to tryptic (proline-blocked). Database search was conducted using the UniProt proteome - `Ecoli_UP000000625_83333`. The minimum peptide length was 7 amino acids. 1% FDR was determined using a reverse decoy proteome.

To calculate the proteome mass fraction of each mapped protein, we utilized the peptide feature information in MaxQuant's `evidence.txt` output file. Each row of the `evidence.txt` file represents an independent peptide and its corresponding MS3 reporter ion measurements. Peptides without signal in any of the TMT channels were excluded. Peptide measurements were assigned to a protein based on MaxQuant's 'Leading razor protein' designation. For each individual peptide measurement (i.e., each row in the evidence table), the fraction of ion intensity in each TMT channel was calculated by dividing the 'Reporter ion intensity' column by the sum of all reporter ion intensities. To correct for loading differences between the TMT channels, each reporter ion channel was then normalized by dividing the fraction of ion intensity in each channel by the median fraction for all measured peptides (i.e., the median value for each column). This normalization scheme ensures that each individual peptide measurement is equally weighted when correcting for loading error. To calculate proteome mass fractions, the MS1 precursor ion intensity of each peptide measured (the "Intensity" column in the `evidence.txt` table) was distributed between the individual MS3 reportion channels according to the loading-normalized value described. Protein-level ion intensities were then calculated for each TMT channel by summing together all peptides ion intensities for each protein.

4.4 Quantification of Total RNA and Protein Masses

The total RNA and total protein measurements needed to calculate the compartment densities in Fig. 2 were measured from cultures independent of those used for mass spectrometry and size quantification.

Briefly, cells were cultured in a basic buffer medium as described above and harvested at an $OD_{600nm} \approx 0.5$. The Biuret method[63] was used for total protein quantification. For each culture, an aliquot of 1.8 mL of cell culture was transferred to a clean 2 mL test tube and were pelleted at 16,000 $\times g$ for 1 minute. The supernatant was removed and the OD_{600nm} was measured to correct for cell los. The pellet was washed with 1 mL of ddH_2O and pelleted again at 16,000 $\times g$. The supernatant was again carefully removed and the OD_{600nm} was determined. The pellet was resuspended in 200 µL of ddH_2O and transferred to a -80 °C freezer for 10 minutes. Once frozen, pellets were transferred to an ice bath and 100 µL of 3M NaOH was added to the pellets, followed by boiling at 100 °C for 5 minutes, followed by a 5 min cool-down at room temperature. A 100 µL aliquot of 1.6% $CuSO_4$ was added to the disrupted cell pellet, shaken vigorously, and incubated at room temperature for 5 min. The slurry was then centrifuged at 16,000 $\times g$ for 3 minutes and the OD_{555nm}. This was converted to a concentration using a calibration curve of known BSA concentrations.

Total RNA quantification was performed as described previously.[64] Briefly, a 1.5 mL aliquot from the steady-state culture was removed and transferred to a 2 mL test tube. Cells were pelleted at 16,000 $\times g$ for 3 min. The supernatant was carefully removed and the OD_{600nm} was determined to correct for cell loss. The pellet was washed twice with 600 µL of 0.7 mM $HClO_4$ at 4 °C with the supernatants pooled and their combined OD_{600nm} determined. The washed pellet was resuspended in 300 µL of 0.3 M KOH and was incubated at 37 °C with shaking for 1 hr. RNA was extracted from the digested cell solution by adding 100 µL of 3M $HClO_4$ and debris was pelleted at 16,000 $\times g$ for 1 min. The supernatant was removed and transferred to a new 2 mL test tube. The debris pellet was washed twice with 550 µL 0.5 M $HClO_4$ kept at 4 °C and supernatants were pooled. The UV absorption of the supernatant at 260nm was measured and total RNA was calculated using a conversion factor of 31 µg / A_{260nm}.

Total cell counts for each growth condition were quantified using flow cytometry. Briefly, cells were grown in the appropriate growth medium to an $OD_{600nm} \approx 0.2 - 0.4$ and 500 µL was transferred to a sterile 1.5 mL eppendorf tube. A volume of fixation buffer (PBS with 0.9% NaCl and 0.12% formaldehyde) was added to the cells and gently mixed. To 810 µL of buffered DAPI (0.9% NaCl with 1 µg/mL DAPI), 100 µL of the above cell sample was added. This was incubated on ice for 3 minutes. Samples were then injected and analyzed in a BD FACSymphony A5 Cell Analyzer with a SSC gain of 1000 and flow rate of 1 µL / s. Signal was collected for 100 seconds per sample. All objects which were DAPI positive were noted as individual cells. We found that applying an automated gating procedure (described in Razo-Mejia *et al.*[65]) did not significantly influence our estimate of cells per unit biomass.

4.5 Quantification of Cellular Growth Rate

During the steady-state growth, the OD_{600nm} was measured at regular intervals using a Thermo Scientific GENESYS 30 Spectrophotometer. For each growth cycle, the growth rate was determined by performing a linear regression on the log-transformed optical density measurements within the linear range of the spectrophotometer (0.04 - 0.5 for our specific spectrophotometer). This was performed on a per-replicate basis and the results of the fitting were saved and collated as a CSV file. The linear regression was performed using the `linregress` function in the Python `scipy.stats` library (version `1.10.0`) using default parameters.

4.6 Localization Annotation of Proteomic Data

The localization of each protein detected within our mass spectrometry measurements was determined using the localization criteria defined in Babu *et al.* 2018.[31] Proteins detected in our experiments yet not annotated or located within the Babu *et al.* annotation form were dropped from all subsequent analysis. In total, this occurred only for 14 proteins accounting for at most 0.1% of the total proteome mass.

4.7 Calculation of Compartment Densities

In this work, we used bulk-measurements of total protein and total RNA coupled with partitioning information from our quantitative mass spectrometry measurements to estimate the protein masses and densities within each compartment for our wild-type *E. coli* strains [Fig. S4(A)]. For each compartment, the total

protein mass in each compartment $M_{prot}^{(compartment)}$ was calculated as

$$M_{prot}^{(compartment)} = \psi_{compartment} M_{prot}^{(tot)} \tag{5}$$

where $\psi_{compartment}$ denotes the proteome partitioning to that compartment and $M_{prot}^{(tot)}$ denotes the total protein mass per cell, determined from bulk measurements. However, we did not directly measure the total protein per cell for each mass spectrometry measurement. To do so, we instead assumed that the total protein per cell scaled exponentially as a function of the growth rate λ, and used the resulting fit to estimate the total protein per cell for samples subjected to mass spectrometry quantification given their measured growth rate. To perform this fit, we used a Bayesian inferential model to compute the posterior distribution over the parameters of the exponential fit as well as the expected homoskedastic measurement error. Details of this inference, along with choice of priors and appropriate transformations, are given in the Appendix. The result of this fit is shown in Fig. S4(B).

For the cytoplasmic density, we made the well-justified assumption that the majority of cytoplasmic mass is composed of protein and RNA[4,41] with DNA contributing a negligible fraction of the mass. Thus, the cytoplasmic density was defined by the proteome mass of the cytoplasm *and* the total cellular RNA. As in the case of total protein, we did not directly measure total RNA for every sample subjected to mass spectrometry. We assumed that the total RNA mass per cell $M_{RNA}^{(tot)}$ also scaled exponentially with the cellular growth rate and used the resulting fit to estimate the RNA for our samples subjected to mass spectrometry. We also used a Bayesian inferential model for this estimation, described in the appendix. The resulting fit is shown in Fig. S4(C).

4.8 Bayesian Inference

Throughout this work, we use Bayesian inferential models to quantify our uncertainty in our estimate of a quantity, such as the compartment densities or the density ratio parameter κ. While details change from model-to-model, the same basic approach applies which we outline here. We adopt a Bayesian definition of probability and seek to evaluate the posterior probability distribution $g(\theta \mid y)$ of a parameter θ conditioned on a set of measurements y. Using Bayes' theorem, this can be computed as

$$g(\theta \mid y) = \frac{f(y \mid \theta) g(\theta)}{f(y)}, \tag{6}$$

where g and f denote probability density functions over parameters and data, respectively. For the data observed in this work, we used a Gaussian distribution for the likelihood function $f(y \mid \theta)$ for the parameter(s) of interest with a model-dependent mean μ and standard deviation σ. The choice of prior distribution $g(\theta)$ was dependent on the precise parameter being inferred (see Appendix). For this work, the denominator $f(y)$ of Eq. 6 was treated as a normalization constant and was therefore neglected in the estimation. All statistical modeling and parameter inference was performed using Markov chain Monte Carlo (MCMC). Specifically, we used Hamiltonian Monte Carlo sampling as is implemented in the Stan programming language.[66] To assess the accuracy of our inference, we evaluated the posterior predictive distribution by randomly sampling values from the likelihood function $f(y \mid \theta)$ for each MCMC sample of θ. From this distribution, we then calculated the arithmetic mean and the bounds of the 68% and 95% percentiles which

correspond to approximately 1σ and 2σ of a Gaussian distribution. All statistical models are defined as `Stan` files are available on the paper's GitHub repository github.com/cremerlab/density_maintenance accessible via DOI: 10.5281/zenodo.10048570.

4.9 Calculation of the cytoplasm-membrane density ratio for ppGpp perturbations

In Fig. S5(B), we report the estimated cytoplasm-membrane density ratio for each ppGpp perturbation measurement. To do so for the wildtype strains, we used our inferred trends in the per-cell total protein $M_{prot}^{(tot)}$ and total RNA $M_{RNA}^{(tot)}$ masses as a function of growth rate. However, for our MeshI and RelA perturbation studies, these quantities do not necessarily scale in the same way with the growth rate. Thus, to calculate the cytoplasm-membrane density ratio, we made the well-motivated approximation that the total RNA mass can be calculated as

$$M_{RNA}^{(tot)} \approx \overbrace{\beta\phi_{rib}}^{\sim \frac{M_{RNA}^{(tot)}}{M_{prot}^{(tot)}}} M_{prot}^{(tot)}, \tag{7}$$

where β is a constant of proportionality that can be directly calculated[3] (Appendix). Using this approximation, the cytoplasm-membrane density ratio can be directly computed from the measured partitioning and allocation parameters determined via mass spectrometry and cell size measurements via

$$\frac{\rho_{cyto}}{\sigma_{mem}} \approx \frac{\psi_{cyto} M_{prot}^{(tot)} + \beta\phi_{rib} M_{prot}^{(tot)}}{\psi_{mem} M_{prot}^{(tot)}} \times \frac{A_{mem}}{V_{cyto}} = \frac{\psi_{cyto} + \beta\phi_{rib}}{\psi_{mem}} \times \frac{2S_A}{V - w_{peri} S_A}, \tag{8}$$

where A_{mem} is the total membrane area, V_{cyto} is the cytoplasmic cell volume, S_A is the cellular surface area, and w_{peri} is the average width of the periplasmic space.

4.10 Code and Data Availability

All Python code, Stan probabilistic models,and processed data sets are available on the paper's GitHub repository DOI:10.5281/zenodo.10048570 accessible via `github.com/cremerlab/density_maintenance`. Raw microscopy images are available to download from the Stanford Data Repository accessible via DOI: 10.25740/ws785mz0287.

4.11 Literature Sources

In this work, we used a large collection of datasets from the literature to evaluate the consistency of our measurements and guide our analysis. These sources are cited where used within the figures. Here, we cite all of these sources for proper referencing and bibliometrics: proteomic measurements;[32,67–73] cell size measurements;[18,28,74–77] Total protein, total RNA, and RNA/protein.[3–5,14,18,28,29,34,41,78–84]

5 Acknowledgements

We thank Markus Arnoldini, Rohan Balakrishnan, Nathan Belliveau, Avi Flamholz, Mathis Leblanc, Shaili Mathur, Manuel Razo-Mejia, Tom Röschinger, Gabe Salmon, Masaru Shimasawa, Jan Skotheim, Alfred Spormann, and the three anonymous reviewers for extensive discussion and critical feedback on the manuscript. We also thank Ferhat Büke and Sander Tans for providing access to data from their recent work.[45] This research was funded in part by the National Institute of General Medical Sciences, National Institutes of Health, grant number 1R01GM149611. G.C. acknowledges support by the NSF Postdoctoral Research Fellowships in Biology Program (grant no. 2010807). J.C. acknowledges support via Bio-X Seeding Grant 10-32 and a Terman Fellowship from Stanford University, USA.

6 Supplemental Figures

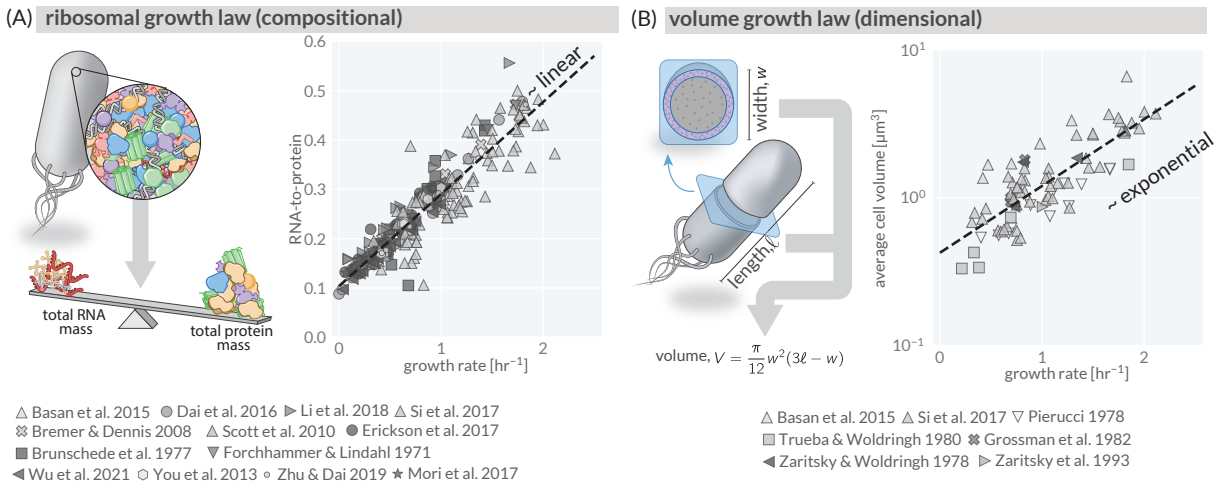

Figure S1: The compositional and geometric growth laws of *E. coli*. (A) The compositional growth law–also termed the "nutrient growth law"–noting that the bulk RNA-to-protein ratio scales approximately linearly with the steady-state growth rate. (B) The volume growth law noting that *E. coli*'s average cell volume scales approximately exponentially with the bulk growth rate. Dashed lines represent empirically-determined regressions to pooled data sets. Complete references for all data given in Methods.

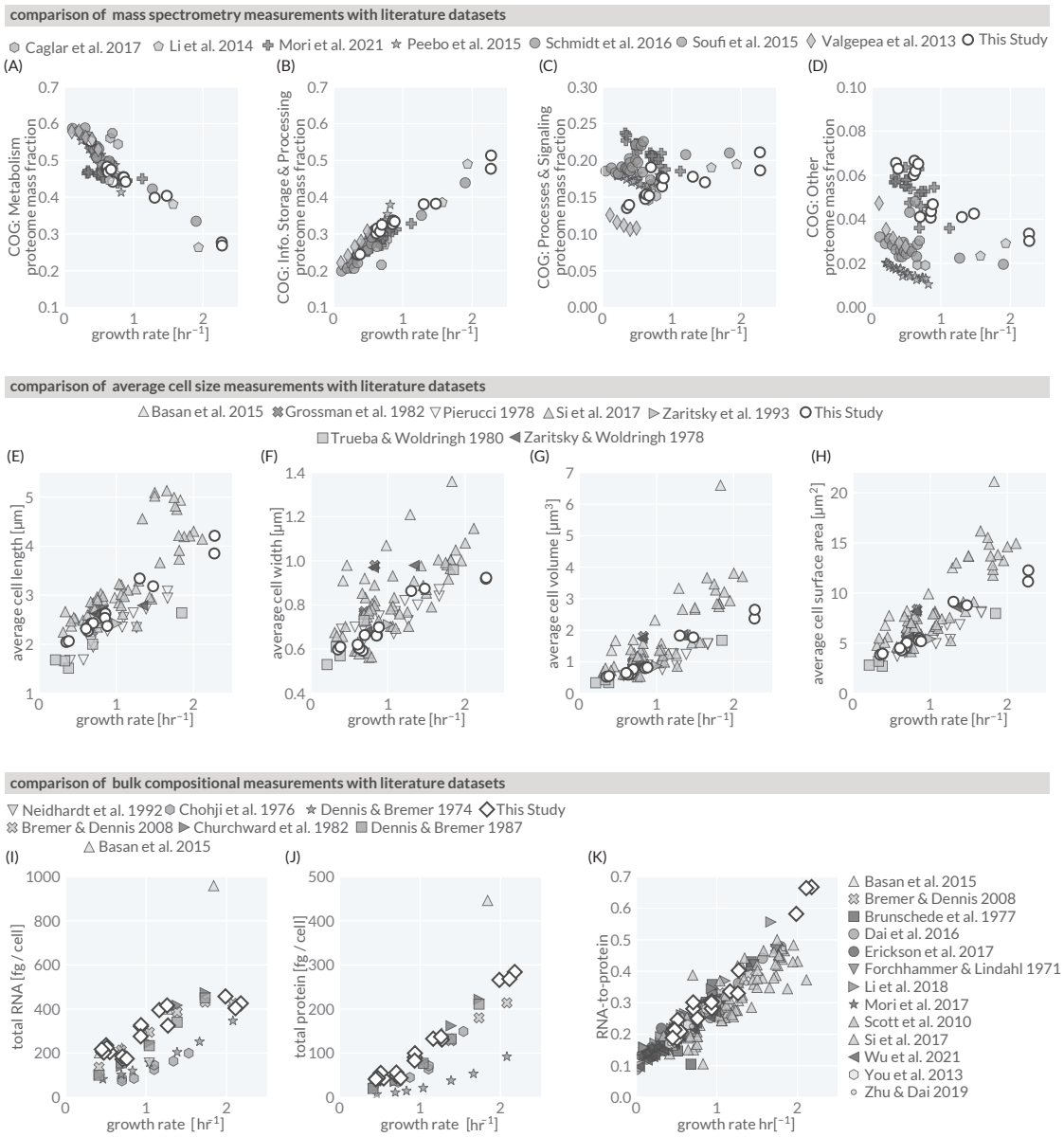

Figure S2: Comparison of measurements from this study with those from the literature. (A–D) Comparison of mass spectrometry measurements from this study (white-faced circles) with reported literature *E. coli* proteomics data, grouped by Clusters of Orthologous Groups (COG[85]) functional annotation. (A) Metabolism; COG Letters: C, G, E, F, H, I, P, Q. (B) Information storage and processing; COG Letters: J, A, K, L, B. (C) Cellular processes and signaling; COG letters: D, Y, V, T, M, N, Z, W, U, O. (D) Other; COG Letters: R, S. (E–H) Comparison of average cell dimensions from this study (white-faced circles) and literature studies (markers). (I–K) Comparison of bulk biochemical measurements from this study (white-faced diamonds) with literature measurements. Citations for literature studies are provided in methods.

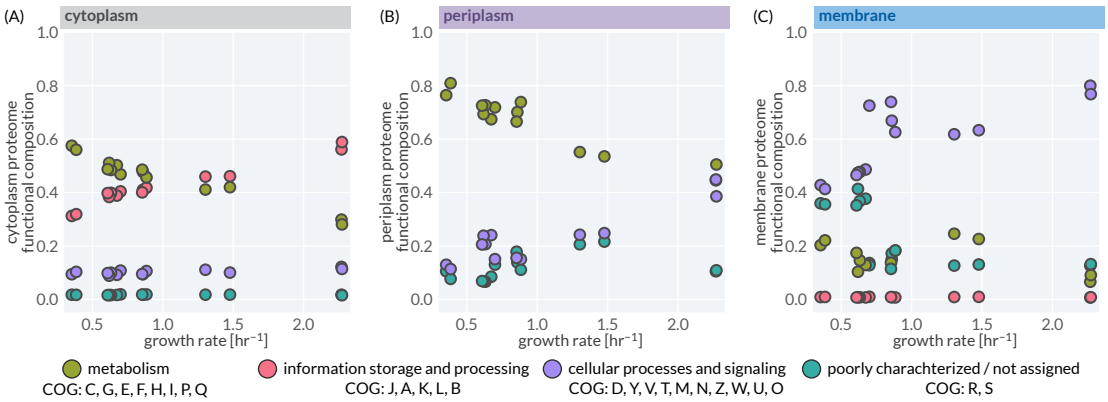

Figure S3: Functional composition of proteomics data within different compartments. Total fraction of proteome occupied by each COG category in the (A) cytoplasm, (B) periplasm, and (C) membranes. COG categories are the same as described in Fig. S2.

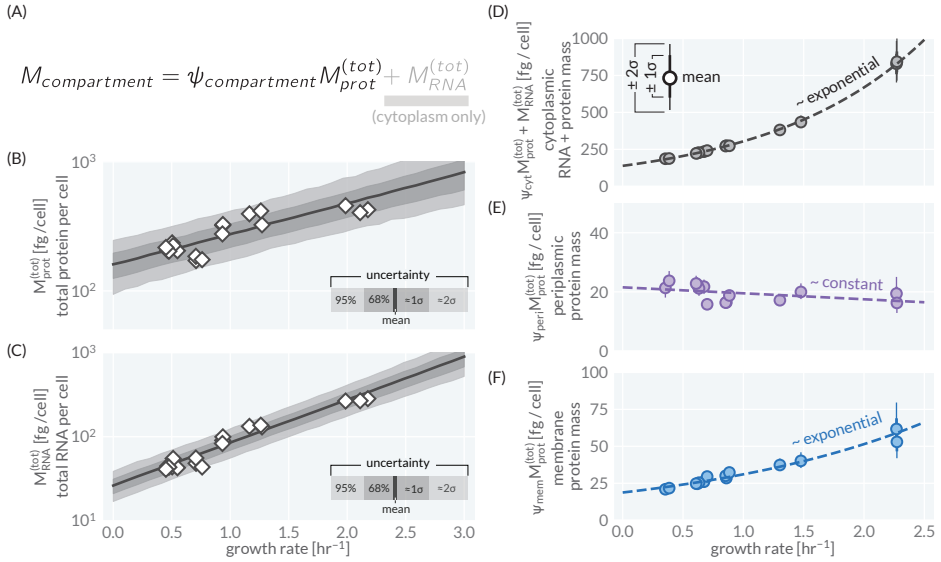

Figure S4: Total compartment masses per cell. (A) The mass of a compartment $M_{compartment}$ is defined as the product of the proteome allocation $\psi_{compartment}$ with the total per-cell protein mass $M_{prot}^{(tot)}$. For the cytoplasm, total mass includes the total RNA mass M_{RNA}. (B) Total protein per cell and (C) total RNA per cell measured in bulk for this study are shown as white-diamonds. Shaded regions correspond to the credible regions of the Bayesian statistical model described in the Appendix. (E) Total RNA + protein mass within the cytoplasm as a function of growth rate. (F) Total protein mass within the periplasm as a function of growth rate. (G) Total protein mass within the membranes as a function of growth rate. Points denote the mean of the posterior probability distribution estimated for each quantity. Thin and thick error bars denote the extent of $\pm$ 2 σ and $\pm$ 1 σ of the posterior distribution. Dashed lines correspond to empirical fits to the posterior means. Cytoplasmic and membrane masses assumed to scale exponentially with the growth rate while the periplasmic mass was assumed to scale linearly.

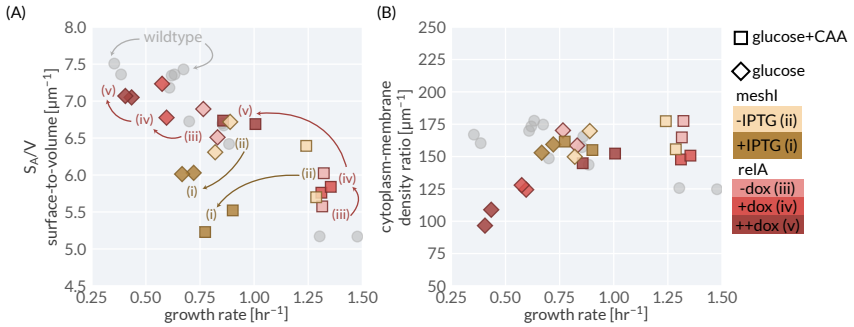

Figure S5: Changes in S_A/V and the cytoplasm-membrane density ratio under perturbation of intracellular ppGpp concentrations (A) Perturbations of intracellular ppGpp concentrations break the dependence of S_A/V on growth rate. The measured surface-to-volume ratio S_A/V is plotted as a function of the steady-state growth rate. MeshI induction in glucose (diamonds) and glucose+CAA (squares) is denoted as trajectory $(ii) \rightarrow (i)$ while RelA induction in each condition is denoted as trajectory $(iii) \rightarrow (iv) \rightarrow (v)$, following the notation shown in Fig. 4. Induction of MeshI (dark gold) decreases both the growth rate and the S_A/V strongly deviating from the wildtype trend. (B) Empirically determined cytoplasm-membrane density ratio for ppGpp perturbation experiments as calculated in Eq. 8. Values for ppGpp perturbation strains are shown in colors and were calculated as described in Methods. MeshI was induced with IPTG ($-$: 0 μM $+$: 100 μM) and RelA was induced with doxycycline ($-$: 0 ng/mL; $+$: 2 ng/mL, $++$: 4 ng/mL).

References

[1] Suckjoon Jun, Fangwei Si, Rami Pugatch, and Matthew Scott. Fundamental principles in bacterial physiology - history, recent progress, and the future with focus on cell size control: a review. *Reports on Progress in Physics*, 81(5):056601, May 2018.

[2] Arthur L. Koch. The Adaptive Responses of Escherichia coli to a Feast and Famine Existence. In A. H. Rose and J. F. Wilkinson, editors, *Advances in Microbial Physiology*, volume 6, pages 147–217. Academic Press, January 1971.

[3] Matthew Scott, Carl W. Gunderson, Eduard M. Mateescu, Zhongge Zhang, and Terence Hwa. Interdependence of Cell Growth and Gene Expression: Origins and Consequences. *Science*, 330(6007):1099–1102, November 2010. tex.ids: scott2010a Publisher: American Association for the Advancement of Science Section: Report.

[4] Jes Forchhammer and Lasse Lindahl. Growth rate of polypeptide chains as a function of the cell growth rate in a mutant of Escherichia coli. *Journal of Molecular Biology*, 55(3):563–568, February 1971.

[5] H Brunschede, T L Dove, and H Bremer. Establishment of Exponential Growth After a Nutritional Shift-Up in *Escherichia coli* B/r: Accumulation of Deoxyribonucleic Acid, Ribonucleic Acid, and Protein. *Journal of Bacteriology*, 129:14, 1977.

[6] Nicole C. E. Imholz, Marek J. Noga, Niels J. F. van den Broek, and Gregory Bokinsky. Calibrating the Bacterial Growth Rate Speedometer: A Re-evaluation of the Relationship Between Basal ppGpp, Growth, and RNA Synthesis in Escherichia coli. *Frontiers in Microbiology*, 11, 2020.

[7] Douwe Molenaar, Rogier van Berlo, Dick de Ridder, and Bas Teusink. Shifts in growth strategies reflect tradeoffs in cellular economics. *Molecular Systems Biology*, 5(1):323, January 2009. Publisher: John Wiley & Sons, Ltd.

[8] M. Scott, S. Klumpp, E. M. Mateescu, and T. Hwa. Emergence of robust growth laws from optimal regulation of ribosome synthesis. *Molecular Systems Biology*, 10(8):747–747, August 2014.

[9] Evert Bosdriesz, Douwe Molenaar, Bas Teusink, and Frank J. Bruggeman. How fast-growing bacteria robustly tune their ribosome concentration to approximate growth-rate maximization. *The FEBS Journal*, 282(10):2029–2044, 2015. _eprint: https://febs.onlinelibrary.wiley.com/doi/pdf/10.1111/febs.13258.

[10] Nils Giordano, Francis Mairet, Jean-Luc Gouzé, Johannes Geiselmann, and Hidde de Jong. Dynamical Allocation of Cellular Resources as an Optimal Control Problem: Novel Insights into Microbial Growth Strategies. *PLOS Computational Biology*, 12(3):e1004802, March 2016. Publisher: Public Library of Science.

[11] Griffin Chure and Jonas Cremer. An optimal regulation of fluxes dictates microbial growth in and out of steady state. *eLife*, 12:e84878, March 2023. Publisher: eLife Sciences Publications, Ltd.

[12] Hugo Dourado and Martin J. Lercher. An analytical theory of balanced cellular growth. *Nature Communications*, 11(1):1226, March 2020. Number: 1 Publisher: Nature Publishing Group.

[13] Andrea Y. Weiße, Diego A. Oyarzún, Vincent Danos, and Peter S. Swain. Mechanistic links between cellular trade-offs, gene expression, and growth. *Proceedings of the National Academy of Sciences*, 112(9):E1038–E1047, March 2015. Publisher: National Academy of Sciences Section: PNAS Plus.

[14] Chenhao Wu, Rohan Balakrishnan, Nathan Braniff, Matteo Mori, Gabriel Manzanarez, Zhongge Zhang, and Terence Hwa. Cellular perception of growth rate and the mechanistic origin of bacterial growth law. *Proceedings of the National Academy of Sciences*, 119(20):e2201585119, May 2022. Publisher: Proceedings of the National Academy of Sciences.

[15] W. D. Donachie, K. J. Begg, and M. Vicente. Cell length, cell growth and cell division. *Nature*, 264(5584):328–333, November 1976. Bandiera_abtest: a Cg_type: Nature Research Journals Number: 5584 Primary_atype: Research Publisher: Nature Publishing Group.

[16] Sattar Taheri-Araghi, Serena Bradde, John T. Sauls, Norbert S. Hill, Petra Anne Levin, Johan Paulsson, Massimo Vergassola, and Suckjoon Jun. Cell-Size Control and Homeostasis in Bacteria. *Current Biology*, 25(3):385–391, February 2015.

[17] Hai Zheng, Po-Yi Ho, Meiling Jiang, Bin Tang, Weirong Liu, Dengjin Li, Xuefeng Yu, Nancy E. Kleckner, Ariel Amir, and Chenli Liu. Interrogating the *Escherichia coli* cell cycle by cell dimension perturbations. *Proceedings of the National Academy of Sciences*, 113(52):15000–15005, December 2016. Company: National Academy of Sciences Distributor: National Academy of Sciences Institution: National Academy of Sciences Label: National Academy of Sciences Publisher: Proceedings of the National Academy of Sciences.

[18] Fangwei Si, Dongyang Li, Sarah E. Cox, John T. Sauls, Omid Azizi, Cindy Sou, Amy B. Schwartz, Michael J. Erickstad, Yonggun Jun, Xintian Li, and Suckjoon Jun. Invariance of Initiation Mass and Predictability of Cell Size in Escherichia coli. *Current Biology*, 27(9):1278–1287, May 2017.

[19] Barak Akabayov, Sabine R. Akabayov, Seung-Joo Lee, Gerhard Wagner, and Charles C. Richardson. Impact of macromolecular crowding on DNA replication. *Nature Communications*, 4(1):1615, March 2013. Number: 1 Publisher: Nature Publishing Group.

[20] Ariel Amir. Is cell size a spandrel? *eLife*, 6:e22186, January 2017. Publisher: eLife Sciences Publications, Ltd.

[21] Manuel Campos, Sander K Govers, Irnov Irnov, Genevieve S Dobihal, François Cornet, and Christine Jacobs-Wagner. Genomewide phenotypic analysis of growth, cell morphogenesis, and cell cycle events in *Escherichia coli*. *Molecular Systems Biology*, 14(6), June 2018. tex.ids: campos2018a.

[22] Leigh K. Harris and Julie A. Theriot. Surface Area to Volume Ratio: A Natural Variable for Bacterial Morphogenesis. *Trends in Microbiology*, 26(10):815–832, October 2018.

[23] Fangwei Si, Guillaume Le Treut, John T. Sauls, Stephen Vadia, Petra Anne Levin, and Suckjoon Jun. Mechanistic Origin of Cell-Size Control and Homeostasis in Bacteria. *Current Biology*, 29(11):1760–1770.e7, June 2019.

[24] Hai Zheng, Yang Bai, Meiling Jiang, Taku A. Tokuyasu, Xiongliang Huang, Fajun Zhong, Yuqian Wu, Xiongfei Fu, Nancy Kleckner, Terence Hwa, and Chenli Liu. General quantitative relations linking cell growth and the cell cycle in Escherichia coli. *Nature Microbiology*, 5(8):995–1001, August 2020. Number: 8 Publisher: Nature Publishing Group.

[25] Sander K. Govers, Manuel Campos, Bhavyaa Tyagi, Géraldine Laloux, and Christine Jacobs-Wagner. Apparent simplicity and emergent robustness in bacterial cell cycle control, January 2023. Pages: 2023.01.16.524295 Section: New Results.

[26] Sriram Tiruvadi-Krishnan, Jaana Männik, Prathitha Kar, Jie Lin, Ariel Amir, and Jaan Männik. Coupling between DNA replication, segregation, and the onset of constriction in Escherichia coli. *Cell Reports*, 38(12):110539, March 2022.

[27] Diana Serbanescu, Nikola Ojkic, and Shiladitya Banerjee. Nutrient-Dependent Trade-Offs between Ribosomes and Division Protein Synthesis Control Bacterial Cell Size and Growth. *Cell Reports*, 32(12), September 2020. Publisher: Elsevier.

[28] Markus Basan, Manlu Zhu, Xiongfeng Dai, Mya Warren, Daniel Sévin, Yi-Ping Wang, and Terence Hwa. Inflating bacterial cells by increased protein synthesis. *Molecular Systems Biology*, 11(10):836, October 2015. Publisher: John Wiley & Sons, Ltd.

[29] Manlu Zhu, Yige Pan, and Xiongfeng Dai. (p)ppGpp: the magic governor of bacterial growth economy. *Current Genetics*, 65(5):1121–1125, October 2019.

[30] Lichao Zhang and Joshua E. Elias. Relative Protein Quantification Using Tandem Mass Tag Mass Spectrometry. In Lucio Comai, Jonathan E. Katz, and Parag Mallick, editors, *Proteomics: Methods and Protocols*, pages 185–198. Springer, New York, NY, 2017.

[31] Mohan Babu, Cedoljub Bundalovic-Torma, Charles Calmettes, Sadhna Phanse, Qingzhou Zhang, Yue Jiang, Zoran Minic, Sunyoung Kim, Jitender Mehla, Alla Gagarinova, Irina Rodionova, Ashwani Kumar, Hongbo Guo, Olga Kagan, Oxana Pogoutse, Hiroyuki Aoki, Viktor Deineko, J. Harry Caufield, Erik Holtzapple, Zhongge Zhang, Ake Vastermark, Yogee Pandya, Christine Chieh-lin Lai, Majida El Bakkouri, Yogesh Hooda, Megha Shah, Dan Burnside, Mohsen Hooshyar, James Vlasblom, Sessandra V. Rajagopala, Ashkan Golshani, Stefan Wuchty, Jack F Greenblatt, Milton Saier, Peter Uetz, Trevor F Moraes, John Parkinson, and Andrew Emili. Global landscape of cell envelope protein complexes in Escherichia coli. *Nature Biotechnology*, 36(1):103–112, January 2018. Number: 1 Publisher: Nature Publishing Group.

[32] Nathan M. Belliveau, Griffin Chure, Christina L. Hueschen, Hernan G. Garcia, Jane Kondev, Daniel S. Fisher, Julie A. Theriot, and Rob Phillips. Fundamental limits on the rate of bacterial growth and their influence on proteomic composition. *Cell Systems*, page S240547122100209X, July 2021.

[33] Sheng Hui, Josh M. Silverman, Stephen S. Chen, David W. Erickson, Markus Basan, Jilong Wang, Terence Hwa, and James R. Williamson. Quantitative proteomic analysis reveals a simple strategy of global resource allocation in bacteria. *Molecular Systems Biology*, 11(2), February 2015. tex.ids: hui2015a.

[34] David W. Erickson, Severin J. Schink, Vadim Patsalo, James R. Williamson, Ulrich Gerland, and Terence Hwa. A global resource allocation strategy governs growth transition kinetics of *Escherichia coli*. *Nature*, 551(7678):119–123, November 2017. tex.ids: erickson2017a Number: 7678 Publisher: Nature Publishing Group.

[35] Rohan Balakrishnan, Roshali T de Silva, Terence Hwa, and Jonas Cremer. Suboptimal resource allocation in changing environments constrains response and growth in bacteria. *Molecular Systems Biology*, 17(12):e10597, December 2021. Publisher: John Wiley & Sons, Ltd.

[36] Alexander M. Berezhkovskii and Attila Szabo. Theory of Crowding Effects on Bimolecular Reaction Rates. *The Journal of Physical Chemistry B*, 120(26):5998–6002, July 2016.

[37] Jose L. Alejo, Christopher P. Kempes, and Katarzyna P. Adamala. Diffusion control in biochemical specificity. *Biophysical Journal*, 121(8):1541–1548, April 2022. Publisher: Elsevier.

[38] K. A. Dill, K. Ghosh, and J. D. Schmit. Physical limits of cells and proteomes. *Proceedings of the National Academy of Sciences*, 108(44):17876–17882, November 2011.

[39] Alexei Vazquez. Optimal macromolecular density in the cell. *Proceedings of the National Academy of Sciences*, 109(9):E533–E533, February 2012. Publisher: Proceedings of the National Academy of Sciences.

[40] Ken A. Dill, Kingshuk Ghosh, and Jeremy Schmit. Reply to Vazquez: Optimal density is robust to variations in calculation. *Proceedings of the National Academy of Sciences*, 109(9):E534–E534, February 2012. Publisher: Proceedings of the National Academy of Sciences.

[41] Hans Bremer and Patrick P. Dennis. Modulation of Chemical Composition and Other Parameters of the Cell at Different Exponential Growth Rates. *EcoSal Plus*, 3(1), October 2008. Publisher: American Society for Microbiology.

[42] Abir T. Asmar, Josie L. Ferreira, Eli J. Cohen, Seung-Hyun Cho, Morgan Beeby, Kelly T. Hughes, and Jean-François Collet. Communication across the bacterial cell envelope depends on the size of the periplasm. *PLOS Biology*, 15(12):e2004303, December 2017. Publisher: Public Library of Science.

[43] M. Schaechter, O. Maaløe, and N. O. Kjeldgaard. Dependency on medium and temperature of cell size and chemical composition during balanced growth of *Salmonella typhimurium*. *Microbiology*, 19(3):592–606, 1958.

[44] Katarzyna Potrykus, Helen Murphy, Nadège Philippe, and Michael Cashel. ppGpp is the major source of growth rate control in E. coli. *Environmental Microbiology*, 13(3):563–575, March 2011.

[45] Ferhat Büke, Jacopo Grilli, Marco Cosentino Lagomarsino, Gregory Bokinsky, and Sander J. Tans. ppGpp is a bacterial cell size regulator. *Current Biology*, 32(4):870–877.e5, February 2022.

[46] T. E. Shehata and A. G. Marr. Effect of temperature on the size of Escherichia coli cells. *Journal of Bacteriology*, 124(2):857, November 1975. Publisher: American Society for Microbiology (ASM).

[47] Francis Mairet, Jean-Luc Gouzé, and Hidde de Jong. Optimal proteome allocation and the temperature dependence of microbial growth laws. *npj Systems Biology and Applications*, 7(1):1–11, March 2021. Number: 1 Publisher: Nature Publishing Group.

[48] Anne Farewell and Frederick C. Neidhardt. Effect of Temperature on In Vivo Protein Synthetic Capacity in *Escherichia coli*. *Journal of Bacteriology*, 180(17):4704–4710, September 1998.

[49] Benjamin D. Knapp and Kerwyn Casey Huang. The Effects of Temperature on Cellular Physiology. *Annual Review of Biophysics*, 51(1):499–526, May 2022.

[50] Abhishek Dey, Venkat Bokka, and Shaunak Sen. Dependence of bacterial growth rate on dynamic temperature changes. *IET Systems Biology*, 14(2):68–74, April 2020.

[51] Susana Matamouros, Thomas Gensch, Martin Cerff, Christian C. Sachs, Iman Abdollahzadeh, Johnny Hendriks, Lucas Horst, Niklas Tenhaef, Julia Tenhaef, Stephan Noack, Michaela Graf, Ralf Takors, Katharina Nöh, and Michael Bott. Growth-rate dependency of ribosome abundance and translation elongation rate in Corynebacterium glutamicum differs from that in Escherichia coli. *Nature Communications*, 14(1):5611, September 2023. Number: 1 Publisher: Nature Publishing Group.

[52] Johannes B. Müller, Philipp E. Geyer, Ana R. Colaço, Peter V. Treit, Maximilian T. Strauss, Mario Oroshi, Sophia Doll, Sebastian Virreira Winter, Jakob M. Bader, Niklas Köhler, Fabian Theis, Alberto Santos, and Matthias Mann. The proteome landscape of the kingdoms of life. *Nature*, 582(7813):592–596, June 2020. Number: 7813 Publisher: Nature Publishing Group.

[53] Sven van Teeffelen and Lars D. Renner. Recent advances in understanding how rod-like bacteria stably maintain their cell shapes. Technical Report 7:241, F1000Research, February 2018. Type: article.

[54] Ethan C. Garner. Toward a Mechanistic Understanding of Bacterial Rod Shape Formation and Regulation. *Annual Review of Cell and Developmental Biology*, 37(1):1–21, 2021. _eprint: https://doi.org/10.1146/annurev-cellbio-010521-010834.

[55] Patricia D.A. Rohs and Thomas G. Bernhardt. Growth and division of the peptidoglycan matrix. *Annual Review of Microbiology*, 75(1):315–336, 2021. PMID: 34351794.

[56] S. Anisah Alyahya, Roger Alexander, Teresa Costa, Adriano O. Henriques, Thierry Emonet, and Christine Jacobs-Wagner. Rodz, a component of the bacterial core morphogenic apparatus. *Proceedings of the National Academy of Sciences*, 106(4):1239–1244, 2009.

[57] Sven van Teeffelen, Siyuan Wang, Leon Furchtgott, Kerwyn Casey Huang, Ned S. Wingreen, Joshua W. Shaevitz, and Zemer Gitai. The bacterial actin mreb rotates, and rotation depends on cell-wall assembly. *Proceedings of the National Academy of Sciences*, 108(38):15822–15827, 2011.

[58] Cyrille Billaudeau, Arnaud Chastanet, Zhizhong Yao, Charlène Cornilleau, Nicolas Mirouze, Vincent Fromion, and Rut Carballido-López. Contrasting mechanisms of growth in two model rod-shaped bacteria. *Nature Communications*, 8(1):15370, Jun 2017.

[59] Nikolay Ouzounov, Jeffrey P. Nguyen, Benjamin P. Bratton, David Jacobowitz, Zemer Gitai, and Joshua W. Shaevitz. Mreb orientation correlates with cell diameter in escherichia coli. *Biophysical Journal*, 111(5):1035–1043, 2016.

[60] Alexandre Colavin, Handuo Shi, and Kerwyn Casey Huang. Rodz modulates geometric localization of the bacterial actin mreb to regulate cell shape. *Nature Communications*, 9(1):1280, Mar 2018.

[61] Randy M. Morgenstein, Benjamin P. Bratton, Jeffrey P. Nguyen, Nikolay Ouzounov, Joshua W. Shaevitz, and Zemer Gitai. RodZ links MreB to cell wall synthesis to mediate MreB rotation and robust morphogenesis. *Proceedings of the National Academy of Sciences*, 112(40):12510–12515, October 2015. Publisher: Proceedings of the National Academy of Sciences.

[62] Eric Soupene, Wally C. van Heeswijk, Jacqueline Plumbridge, Valley Stewart, Daniel Bertenthal, Haidy Lee, Gyaneshwar Prasad, Oleg Paliy, Parinya Charernnoppakul, and Sydney Kustu. Physiological studies of Escherichia coli strain MG1655: growth defects and apparent cross-regulation of gene expression. *Journal of Bacteriology*, 185(18):5611–5626, September 2003.

[63] D. Herbert, P.J. Phipps, and R.E. Strange. Chapter iii chemical analysis of microbial cells. volume 5 of *Methods in Microbiology*, pages 209–344. Academic Press, 1971.

[64] S. Benthin, J. Nielsen, and J. Villadsen. A simple and reliable method for the determination of cellular rna content. *Biotechnology Techniques*, 5(1):39–42, Jan 1991.

[65] Manuel Razo-Mejia, Stephanie L. Barnes, Nathan M. Belliveau, Griffin Chure, Tal Einav, Mitchell Lewis, and Rob Phillips. Tuning transcriptional regulation through signaling: A predictive theory of allosteric induction. *Cell Systems*, 6(4):456–469.e10, April 2018. Citation Key Alias: razo-mejia, razo-mejia2018d.

[66] Bob Carpenter, Andrew Gelman, Matthew D. Hoffman, Daniel Lee, Ben Goodrich, Michael Betancourt, Marcus Brubaker, Jiqiang Guo, Peter Li, and Allen Riddell. Stan: A probabilistic programming language. *Journal of Statistical Software*, 76(1):1–32, January 2017.

[67] Mehmet U. Caglar, John R. Houser, Craig S. Barnhart, Daniel R. Boutz, Sean M. Carroll, Aurko Dasgupta, Walter F. Lenoir, Bartram L. Smith, Viswanadham Sridhara, Dariya K. Sydykova, Drew Vander Wood, Christopher J. Marx, Edward M. Marcotte, Jeffrey E. Barrick, and Claus O. Wilke. The E. coli molecular phenotype under different growth conditions. *Scientific Reports*, 7(1):1–15, April 2017.

[68] Gene-Wei Li, David Burkhardt, Carol Gross, and Jonathan S. Weissman. Quantifying absolute protein synthesis rates reveals principles underlying allocation of cellular resources. *Cell*, 157(3):624–635, April 2014.

[69] Matteo Mori, Zhongge Zhang, Amir Banaei-Esfahani, Jean-Benoît Lalanne, Hiroyuki Okano, Ben C Collins, Alexander Schmidt, Olga T Schubert, Deok-Sun Lee, Gene-Wei Li, Ruedi Aebersold, Terence Hwa, and Christina Ludwig. From coarse to fine: the absolute *Escherichia coli* proteome under diverse growth conditions. *Molecular Systems Biology*, 17(5), May 2021.

[70] Karl Peebo, Kaspar Valgepea, Andres Maser, Ranno Nahku, Kaarel Adamberg, and Raivo Vilu. Proteome reallocation in *Escherichia coli* with increasing specific growth rate. *Molecular BioSystems*, 11(4):1184–1193, 2015.

[71] Alexander Schmidt, Karl Kochanowski, Silke Vedelaar, Erik Ahrné, Benjamin Volkmer, Luciano Callipo, Kèvin Knoops, Manuel Bauer, Ruedi Aebersold, and Matthias Heinemann. The quantitative and condition-dependent *Escherichia coli* proteome. *Nature Biotechnology*, 34(1):104–110, January 2016.

[72] Boumediene Soufi, Karsten Krug, Andreas Harst, and Boris Macek. Characterization of the *E. coli* proteome and its modifications during growth and ethanol stress. *Frontiers in Microbiology*, 6, February 2015. tex.ids: soufi2015a.

[73] Kaspar Valgepea, Kaarel Adamberg, Andrus Seiman, and Raivo Vilu. Escherichia coli achieves faster growth by increasing catalytic and translation rates of proteins. *Molecular BioSystems*, 9(9):2344–2358, July 2013. Publisher: The Royal Society of Chemistry.

[74] N Grossman, E Z Ron, and C L Woldringh. Changes in cell dimensions during amino acid starvation of Escherichia coli. *Journal of Bacteriology*, 152(1):35–41, October 1982.

[75] Arieh Zaritsky, Conrad L. Woldringh, Charles E. Helmstetter, and N. B. Grover. Dimensional rearrangement of Escherichia coli B/r cells during a nutritional shift-down. *Microbiology*, 139(11):2711–2714, 1993. Publisher: Microbiology Society,.

[76] F J Trueba and C L Woldringh. Changes in cell diameter during the division cycle of Escherichia coli. *Journal of Bacteriology*, 142(3):869–878, June 1980. Publisher: American Society for Microbiology.

[77] A. Zaritsky and C. L. Woldringh. Chromosome replication rate and cell shape in *Escherichia coli*: lack of coupling. *Journal of Bacteriology*, 135(2):581–587, August 1978.

[78] P. P. Dennis and H. Bremer. Macromolecular composition during steady-state growth of Escherichia coli B-r. *Journal of Bacteriology*, 119(1):270–281, July 1974.

[79] Gordon Churchward, Hans Bremer, and Ry Young. Macromolecular composition of bacteria. *Journal of Theoretical Biology*, 94(3):651–670, February 1982.

[80] H Bremer and Patrick P. Dennis. *Modulation of chemical composition and other parameters of the cell by growth rate. Neidhardt, et al. eds. Escherichia coli and Salmonella typhimurium: Cellular and Molecular Biology, 1st ed. chapter 96, Table 2 pp.1530-1*. Escherichia coli and Salmonella typhimurium: Cellular and Molecular Biology,. 1 edition, 1987.

[81] Xiongfeng Dai, Manlu Zhu, Mya Warren, Rohan Balakrishnan, Vadim Patsalo, Hiroyuki Okano, James R. Williamson, Kurt Fredrick, Yi-Ping Wang, and Terence Hwa. Reduction of translating ribosomes enables Escherichia coli to maintain elongation rates during slow growth. *Nature Microbiology*, 2(2):1–9, December 2016. Number: 2 Publisher: Nature Publishing Group.

[82] T Chohji, T Sawada, and S Kuno. Macromolecule synthesis in Escherichia coli BB under various growth conditions. *Applied and Environmental Microbiology*, 31(6):864–869, June 1976.

[83] Conghui You, Hiroyuki Okano, Sheng Hui, Zhongge Zhang, Minsu Kim, Carl W. Gunderson, Yi-Ping Wang, Peter Lenz, Dalai Yan, and Terence Hwa. Coordination of bacterial proteome with metabolism

by cyclic AMP signalling. *Nature*, 500(7462):301–306, August 2013. Bandiera_abtest: a Cg_type: Nature Research Journals Number: 7462 Primary_atype: Research Publisher: Nature Publishing Group Subject_term: Bacteriology;Systems analysis Subject_term_id: bacteriology;systems-analysis.

[84] Sophia Hsin-Jung Li, Zhiyuan Li, Junyoung O. Park, Christopher G. King, Joshua D. Rabinowitz, Ned S. Wingreen, and Zemer Gitai. Escherichia coli translation strategies differ across carbon, nitrogen and phosphorus limitation conditions. *Nature Microbiology*, 3(8):939–947, August 2018. Bandiera_abtest: a Cg_type: Nature Research Journals Number: 8 Primary_atype: Research Publisher: Nature Publishing Group Subject_term: Bacterial physiology;Bacterial systems biology;Dynamical systems Subject_term_id: bacterial-physiology;bacterial-systems-biology;dynamical-systems.

[85] Michael Y. Galperin, Yuri I. Wolf, Kira S. Makarova, Roberto Vera Alvarez, David Landsman, and Eugene V. Koonin. COG database update: focus on microbial diversity, model organisms, and widespread pathogens. *Nucleic Acids Research*, 49(D1):D274–D281, January 2021.